Chemical Science

ROYAL SOCIETY OF CHEMISTRY

EDGE ARTICLE

View Article Online
View Journal | View Issue

Cite this: *Chem. Sci.*, 2024, **15**, 14228

All publication charges for this article have been paid for by the Royal Society of Chemistry

Bridging polymer architecture, printability, and properties by digital light processing of block copolycarbonates†

Krista G. Schoonover, ‡[a] Chia-Min Hsieh, ‡[a] Mani Sengoden, [a] Naushad Ahmed, [a] Manivannan Sivaperuman Kalairaj, [b] Taylor H. Ware, [bc] Donald J. Darensbourg, *[a] Emily B. Pentzer *[ac] and Peiran Wei *[d]

CO_2-based aliphatic polycarbonates (aPCs), produced through the alternating copolymerization of epoxides with CO_2, present an appealing option for sustainable polymeric materials owing to their renewable feedstock and degradable characteristics. An ongoing challenge in working with aPCs is modifying their mechanical properties to meet specific demands. Herein, we report that monomer ratio and polymer architecture of aPCs impact not only printability by digital light processing (DLP) additive manufacturing, but also dictate the thermomechanical and degradation properties of the printed objects. We found that block copolymers exhibit tailorable thermomechanical properties ranging from soft elastomeric to strong and brittle as the proportion of hard blocks increases, whereas the homopolymer blend failed to print objects and statistical copolymers delaminated or overcured, displaying the weakest mechanical properties. In addition, the hydrolytic degradation of the prints was demonstrated under various conditions, revealing that BCP prints containing a higher proportion of hard blocks had slower degradation and that statistical copolymer prints degraded more slowly than their BCP counterparts. This study underscores that polymer composition and architecture both play key roles in resin printability and bulk properties, offering significant prospects for advancing sustainable materials in additive manufacturing through polymer design.

Received 10th July 2024
Accepted 1st August 2024

DOI: 10.1039/d4sc04593a

rsc.li/chemical-science

Introduction

Aliphatic polycarbonates (aPCs) have garnered significant attention in attempts to enhance sustainability of polymeric materials because they offer dual sustainability benefits by utilizing the greenhouse gas CO_2 as a feedstock and featuring hydrolytically degradable linkages.[1–3] In the past few decades, the bisphenol A-free and biodegradable characteristics of aPCs have highlighted their appeal as materials for biomedical engineering and drug delivery systems.[1,4,5] Historically, due to their aliphatic structure, aPCs have primarily been utilized as precursors to polyurethane foams;[6–8] packaging materials;[3,9] surfactants for emulsions;[10,11] or processed into fibers or deposited onto substrates as films.[12,13] Indeed, relatively few studies report the production of bulk aPCs with robust thermomechanical properties.[14,15]

aPCs can be synthesized by the ring-opening polymerization (ROP) of cyclic carbonates, particularly functionalized trimethylene carbonate (TMC), or the ring-opening copolymerization (ROCOP) of CO_2 with epoxides or oxetanes.[16] Advances in polymerization techniques, such as catalyst development for faster polymerizations or under milder conditions, along with the introduction of functional monomers, have expanded the available aPCs, offering a diverse range of chemical compositions and structures.[17,18] Moreover, new functionalities and improved material properties of aPCs have been achieved through the design and synthesis of block copolymers (BCPs), specifically with polyesters and polyethers.[19–21]

Over the past two decades, additive manufacturing (AM), also known as 3D printing (3DP), has expanded the possible applications of polymeric materials by enabling the integration of polymers and their composites into objects with complex and custom geometries.[22] Although AM techniques have been broadly reported, their application for processing aPCs only began in late 2014, predominantly focusing on biomedical applications such as tissue scaffolds.[23–30] In 2015, Liu Wen-Guang and coworkers prepared bone scaffolds from

[a]*Department of Chemistry, Texas A&M University, 3255 TAMU, College Station, TX 77843, USA. E-mail: djdarens@chem.tamu.edu; emilypentzer@tamu.edu*

[b]*Department of Biomedical Engineering, Texas A&M University, 3003 TAMU, College Station, TX 77843, USA*

[c]*Department of Materials Science and Engineering, Texas A&M University, 3003 TAMU, College Station, TX 77843, USA*

[d]*Soft Matter Facility, Texas A&M University, College Station, TX 77843, USA. E-mail: peiran@tamu.edu*

† Electronic supplementary information (ESI) available. See DOI: https://doi.org/10.1039/d4sc04593a

‡ These two authors contributed equally.

commercially available aPC with hydroxyapatite (HA) additive by selective laser sintering (SLS), a 3DP technique where layers of powder are thermally sintered in a desired pattern.[30] This approach gave tunable porosity, microstructure, and mechanical properties based on wt% HA and printing conditions, highlighting the synergy of aPCs and 3DP. In 2022, our group reported an extrusion-based direct ink write (DIW) printing of novel CO_2-based aPCs.[31] By dissolving aPC polymers in solvent and adding NaCl particles, thixotropic inks were prepared and printed, then salt and solvent were removed to give hierarchically porous materials. Notably, this work was limited to the production of low-resolution objects and required the use of a particle additive. Complementing SLS and DIW, vat photopolymerization can afford higher resolution and expedited prints. Vat photopolymerization relies on a photo-initiated chemical reaction of liquid resin to produce thermosets; the most common platforms are acrylate and epoxy crosslinking, though thiol–ene click chemistry is increasingly popular.[32] For example, Dove and coworkers applied micro-stereolithography (μSL) to print patient-specific tissue scaffolds with allyl-functional poly(TMC) (PTMC); the authors demonstrated the synergy of a biocompatible aPC and 3DP technique to promote cell viability for a desired bioengineering application.[28] In pursuit of scaffolds with controlled properties, Blanquer and coworkers developed an array of aPC–gelatin hybrid inks for stereolithography (SLA) by grafting PTMC onto gelatin, followed by methacrylation of the polymer end groups to provide crosslinkable handles.[33] By varying the length of PTMC, scaffold properties were tunable between hydrogel and elastomeric.

More recently, copolymers have gained attention as attractive feedstocks due to tunability based on monomer identity, ratio, and sequence, providing access to material properties different to or greater than the sum of individual components. Common copolymer sequences include statistical, diblock, and triblock (*e.g.* ABA or ABC), with homopolymer blends often used for comparison.[34] For example, Dove and coworkers reported allyl- and norbornene-functionalized PTMC statistical copolymers for digital light processing (DLP) printing *via* thiol–ene click chemistry, showcasing enhanced biocompatibility, degradation, and shape memory for tissue engineering applications.[35] The thermomechanical properties of the printed scaffolds were tuned by adjusting monomer ratio, allowing scaffold properties to be tuned for desired application (*e.g.*, soft tissue *vs.* bone scaffold). Compared to statistical copolymers, BCPs exhibit distinct properties because they can phase separate to minimize the free energy, balancing the competing forces of chain stretching and interfacial contact energy.[36,37] BCPs can be directly printed[38–41] or used as additives to produce objects with enhanced properties.[42–44] Goto and coworkers added stimuli-responsive BCP nanoassemblies to commercially available resins and printed by DLP, demonstrating the ability of BCP additives to impart novel functionality to printed objects.[44] However, the relationship between polymer composition, printability, and the resultant thermomechanical properties for crosslinked BCP systems was not well understood. To our knowledge, the closest example of sequence-controlled macromers in 3DP was reported in 2023 by Blasco and coworkers; the authors compared printing conditions and properties of alternating, di- and tri-block polyacrylate oligomers ($N = 8$) using two-photon laser printing.[45] While this work hints at opportunities to use sequence specific oligomers as feedstocks for 3D printing, the fundamental question remains: how does copolymer architecture impact photopolymer printing?

Herein, we demonstrate that the composition and architecture of aPC polymers ($N > 130$) impact their ability to be printed by DLP, as well as the thermal, mechanical, and degradation properties of the resulting printed structures. As demonstrated

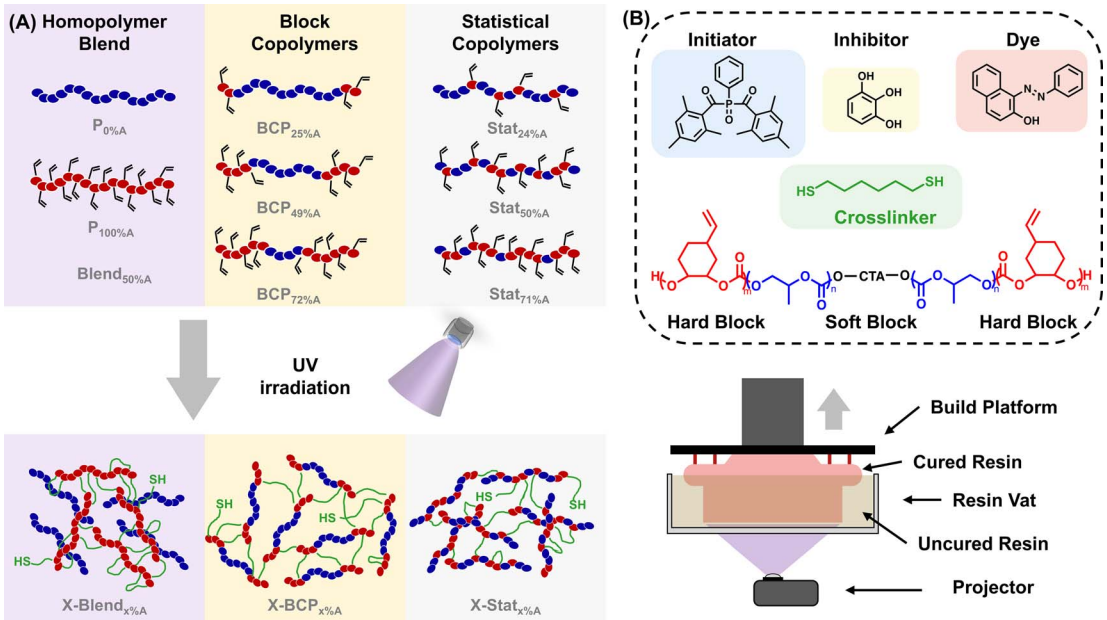

Fig. 1 (A) Schematic of polymer systems printed in this study, highlighting different architectures for pristine and printed polymers and their effect on mechanical properties. (B) Schematic of DLP printing process and identification of resin components.

in Fig. 1A, three monomer ratios for ABA triblock aPCs were used, as well as their corresponding statistical copolymers and a homopolymer blend of similar molar masses and low dispersities. The polymer thermal properties were evaluated by modulated differential scanning calorimetry (MDSC) and thermogravimetric analysis (TGA), with all copolymers decomposing above 230 °C and having glass transition temperatures (T_g's) dependent on monomer ratio and polymer architecture. The printability of seven polymer-based resins was demonstrated using a commercial DLP printer (Fig. 1B) with the resin formulation and printing parameters held constant to evaluate the effect of polymer composition. The fidelity of the printed objects was characterized by optical imaging and scanning electron microscopy (SEM), revealing that all BCPs printed significantly better than the statistical copolymers or homopolymer blend. Thermomechanical properties of the prints, assessed by MDSC, TGA, dynamic mechanical analysis (DMA), and nanoindentation revealed that the printed objects from statistical polymers were weaker than those from the BCPs, with properties varying based on monomer ratio. Finally, variations in composition also influenced hydrolytic degradation, with BCPs containing a higher proportion of hard blocks showing slower degradation, and the statistical copolymers degrading more slowly than BCP counterparts. This work addresses how polymer structure impacts both processing conditions and the properties of the final objects, highlighting how tailored polymer chemistry and architecture can be used to tune thermomechanical and degradation behavior for controlled sustainable performance.

Results and discussion

Synthesis and characterization of aPCs

To determine the impact of polymer composition on the printing process and properties of the printed objects, polymers of similar molar masses and narrow molar mass distributions are ideal. Guided by this, eight distinct polymer samples were prepared, as shown in Fig. 1A: three ABA triblock copolymers, three statistical copolymers, and two homopolymers, all with molar masses of 23 ± 3 kDa and dispersity ($Đ$) < 1.2 (with the exception of $P_{100\%A}$). The polymers were synthesized by the ROCOP of CO_2 with propylene oxide (PO) and vinyl cyclohexene oxide (VCHO). This selection of monomers enables the production of classical ABA hard-soft-hard thermoplastic elastomers: poly(vinyl cyclohexene carbonate) (PVCHC, denoted as A block) has a T_g of 108 °C, and poly(propylene carbonate) (PPC, denoted as B block) has a T_g of 34 °C. Consequently, at ambient temperature, PVCHC is hard ($T < T_g$) and PPC is relatively soft ($T \sim T_g$). These polymers were synthesized by loading the catalyst, cocatalyst, chain transfer agent (CTA, for copolymers only), and epoxide monomer(s) into a stainless-steel reactor under inert conditions, then sealing it and pressurizing with CO_2 before heating (see Experimental for details). To produce ABA block copolymers, VCHO was added after the complete conversion of PO, whereas statistical copolymers were synthesized by the concurrent addition of both monomers. Of note, based on the expected reactivity ratios of PO and VCHO, the statistical polymers likely have a gradient character, with more PO consumed initially.[46] By controlling the feed ratios of monomers and CTA, the desired overall molar mass and mol% PVCHC were achieved to produce: block copolymers $BCP_{25\%A}$, $BCP_{49\%A}$, and $BCP_{72\%A}$; statistical copolymers $Stat_{24\%A}$, $Stat_{50\%A}$, and $Stat_{71\%A}$; and homopolymers $P_{0\%A}$ and $P_{100\%A}$, the latter of which were used to produce a 1 : 1 wt : wt blend termed $Blend_{50\%A}$. Throughout this work, $P_{0\%A}$ and $P_{100\%A}$ refer to the homopolymers themselves, while PPC and PVCHC refer only to the respective polymeric portions of the copolymers. A summary of the composition, molar mass, and thermal properties of the polymer samples is provided in Table 1.

The composition of the aPCs was verified by ^{1}H nuclear magnetic resonance (NMR) and Fourier-transform infrared (FTIR) spectroscopies (see Fig. S1–S9†). As highlighted in Fig. 2A, the relative peak intensities corresponding to the repeat units of each block change in proportion to mol% PVCHC and can be quantified by taking the normalized integration ratio of the methine proton peak of PVCHC (5.7 ppm, signal i) to the methylene proton peak of PPC (4.2 ppm, signal b). Molecular composition was also qualitatively verified by FTIR spectroscopy (Fig. 2B); the asymmetric CH_3 stretching at 2990 cm^{-1} and symmetric bending at 1381 and 1355 cm^{-1} (green shaded box) are indicative of the methyl group in the PC repeat unit, increasing in intensity with increasing PPC content. PVCHC content was supported by the methine CH stretch at 3078 cm^{-1}

Table 1 Characterization of block, statistical, and homo aPCs used as feedstock in DLP

	Polymer composition					Thermal properties	
Polymer	PC : VCHC[a]	M_n[b] (kDa)	$Đ$[b]	D_{avg}[c] ($\times 10^{-10}$ m^2 s^{-1})	M_w[c] (kDa)	T_g[d] (°C)	T_d[e] (°C)
$P_{0\%A}$	1 : 0	26.7	1.11	1.06 ± 0.02	22.8	34	250
$P_{100\%A}$	0 : 1	23.0	1.37	1.11 ± 0.01	20.6	108	315
$Blend_{50\%A}$	1 : 1	—	—	1.09 ± 0.04	21.5	36, 113	237, 303
$BCP_{25\%A}$	3.05 : 1	23.2	1.18	1.16 ± 0.03	18.7	34	278
$BCP_{49\%A}$	1.03 : 1	23.7	1.14	1.16 ± 0.02	18.7	38, 81	255, 309
$BCP_{72\%A}$	0.39 : 1	21.8	1.12	1.27 ± 0.04	15.4	66	300
$Stat_{24\%A}$	3.22 : 1	20.2	1.14	1.10 ± 0.06	21.3	39	247
$Stat_{50\%A}$	1.01 : 1	20.5	1.12	1.26 ± 0.04	15.7	63	286
$Stat_{71\%A}$	0.40 : 1	24.6	1.20	1.00 ± 0.04	26.1	79	283

[a] Determined by ^{1}H NMR integration. [b] Determined by SEC in THF against PS standards. [c] Determined by DOSY NMR. [d] Determined from the normalized reversing heat flow of MDSC. [e] Defined as peaks of the 1st derivative in TGA.

and vinyl C=C stretch at 1640 cm^{-1} (blue shaded box), as well as the cyclohexyl CH_2 asymmetric stretching frequency at 2939 and 2860 cm^{-1} (yellow shaded box).

The molar masses were obtained by size exclusion chromatography (SEC) and purity confirmed by diffusion-ordered spectroscopy (DOSY) NMR. By SEC, all polymers show an M_n

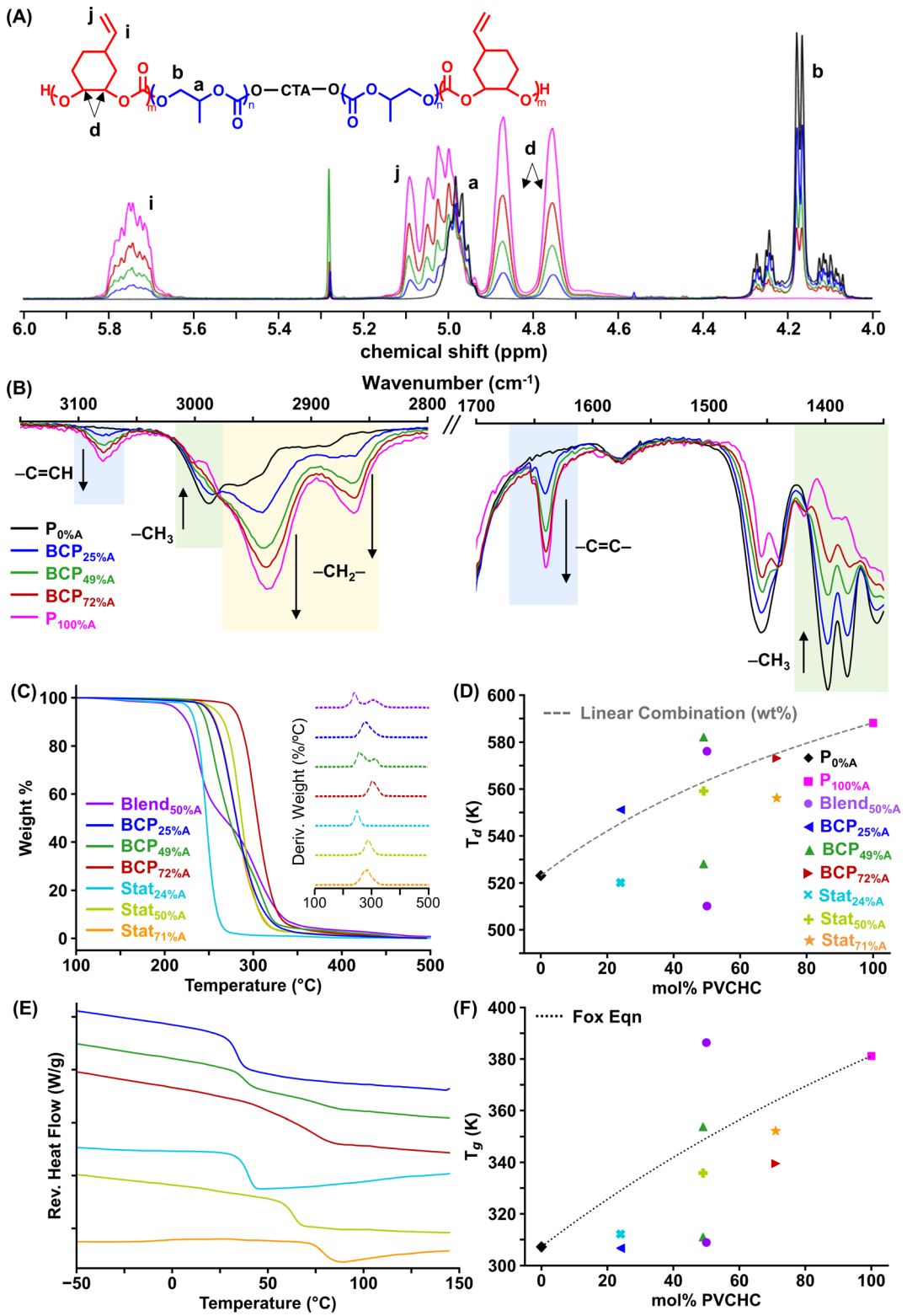

Fig. 2 Chemical and thermal characterization of polymer samples. (A) ^{1}H NMR spectroscopy. (B) FTIR spectroscopy. (C) TGA with inset showing the first derivatives; (D) T_d as a function of mol% PVCHC; (E) MDSC showing the offset normalized reversing heat flow trace; and (F) T_g as a function of mol% PVCHC.

of 23 ± 3 kDa, with monomodal molar mass distributions and narrow dispersity (Fig. S10†); the calculated degrees of polymerization are also comparable across the polymer set (Table S1†). The consistent M_n and low dispersity allow us to investigate the impact of monomer ratio and architecture on printability and properties of the resultant prints. DOSY NMR was used to ensure no homopolymer impurities were present. The average diffusion coefficients (D) with weighted error for each polymer are reported in Table 1 and Fig. S11.† The data reveal that D for all samples had <4% variance across all peaks, indicating no homopolymer impurities;[47] if chain extension of the second block were not successful, then the B block homopolymer would be observed as a significantly larger D than that of the A block for BCPs. Notably, the blend of two homopolymers ($Blend_{50\%A}$) also had low variance, indicating that DOSY cannot detect impurities of comparable molar mass of two polymers. The weight average molar mass (M_w) was also calculated from D for each polymer, comparing to polystyrene standards in $CDCl_3$ as reported by Junkers and coworkers.[48] The M_w values determined from DOSY were generally lower than those measured by SEC, which we attribute to fundamental differences in the techniques and parameters, *e.g.*, solvent and temperature.

Polymer thermal properties

To establish the relationship between polymer composition, macromolecular structure, and polymer properties, the thermal properties of the polymers were characterized. As plotted in Fig. 2C and S12,† TGA weight loss profiles were used to evaluate thermal decomposition of all polymers and establish a suitable temperature range for applications. The decomposition temperature (T_d) is defined as the maximum of the first derivative of the weight loss shown in Fig. 2C inset. As listed in Table 1, $P_{0\%A}$ and $P_{100\%A}$ had the lowest and highest T_d values at 250 °C and 315 °C, respectively, with the T_d values of $Blend_{50\%A}$ consistent with this. Among all the BCPs, only $BCP_{49\%A}$ exhibited two well-separated T_d's, indicating significant microphase separation when the two blocks are of the same ratio (Fig. 2D); notably, $BCP_{25\%A}$ and $BCP_{72\%A}$ have T_d's in agreement with a linear combination of the T_d's of the homopolymers $P_{0\%A}$ and $P_{100\%A}$ (eqn (S1) and Table S2†). $Stat_{24\%A}$ and $Stat_{71\%A}$ have lower T_d's than their BCP counterparts, indicating lower thermal stability for Stat compared to BCP architectures.

T_g's were measured by MDSC; by adding a sinusoidal modulation to the linear temperature ramp, this technique separates the heat flow into a reversible component (heat capacity) and a non-reversible component (kinetic events), which is useful when a polymer exhibits complex thermal behavior. Fig. 2E plots the reverse heat flow for each polymer (individual polymer data in Fig. S13†), and Table 1 summarizes T_g values for the polymers, which range from 34 to ~110 °C. As with T_d's, $Blend_{50\%A}$ had two T_g's consistent with the homopolymers, indicating phase separation, as expected. Of the copolymers, only $BCP_{49\%A}$ had two distinct T_g's, echoing the TGA data. $BCP_{25\%A}$ had a T_g at 34 °C indicating that the PPC dominates, whereas $BCP_{72\%A}$ had a broad transition spanning from 40 to 86 °C. In contrast, all Stat copolymers had narrow T_g's increasing with mol% PVCHC, and each higher than their corresponding BCP (visualized in Fig. 2F). Indeed, Stat copolymers had T_g's closer to those calculated by the Fox equation[49–51] (eqn (S2) and Table S2†), indicating a higher degree of miscibility for Stat than BCP, as expected.

Ink formulation and 3D printing

Resin formulation and printability are critical for high-resolution DLP printing. We formulated all polymers into resins by dissolving the polymer in a 3 : 1 v/v mixture of propylene carbonate and ethyl acetate containing 1,6-hexanedithiol (HDT), initiator, inhibitor, and dye (Fig. 1B). Propylene carbonate was initially chosen as a sustainably sourced and biocompatible solvent (and as previously reported for aPCs),[27,28,52] but its use alone gave resins with high viscosity and a slow cure rate. Thus, ethyl acetate was used as a cosolvent (25 vol%) to decrease resin viscosity while maintaining biocompatibility.[53] All resins were visually transparent except for those formulated with $BCP_{49\%A}$ and $BCP_{72\%A}$ (Fig. 3A), possibly indicating self-assembly in solution (*e.g.*, micelle formation), consistent with the microphase separation observed in the bulk polymer. HDT serves as a crosslinker for thiol–ene reactions with the alkene groups of PVCHC blocks, employing a 1 : 1 molar ratio of thiol to vinyl (see eqn (S2)†). The amounts of photoinitiator, radical inhibitor, and dye were held constant relative to the total resin mass (see Experimental details and Table S3†) so as to enable comparison of the impact of polymer composition and architecture on printing. The inhibitor is necessary to prevent spontaneous initiation of click reactions, and the dye helps absorb additional irradiation, preventing overcuring. To confirm thiol–ene reactions were responsible for cross-linking, a resin was formulated without HDT and subjected to printing conditions; the resin remained liquid-like thus supporting that vinyl self-curing reactions were negligible and thiol–ene reactions accounted for the majority of the printed network (Fig. S14†).

To evaluate the impact of monomer ratio and polymer architecture on printing and resultant prints, all resins were printed using the same parameters without any post-curing step, as outlined in Table S4.† In brief, resins were loaded into a DLP vat (Fig. S15†) and ten 100 μm thick layers were printed by exposing the vat to 405 nm light for 60 s for each layer, resulting in 1 mm thick printed objects. The printing parameters were developed to balance speed, resolution, and layer adhesion. Printed objects resulting from each of these polymers are termed X-$BCP_{x\%A}$, X-$Stat_{x\%A}$, and X-$Blend_{50\%A}$, with printing occurring upon chemical crosslinking of the vinyl group of VCHC repeat units (see Fig. 1A). Notably, $P_{0\%A}$ could not be printed because it has no vinyl groups and the resin formulated with $P_{100\%A}$ was too viscous for printing (but could be bulk cured for comparison). FTIR spectroscopy indicates that DLP-mediated crosslinking did not lead to full consumption of vinyl groups, as seen by residual alkene stretching at 1640 cm^{-1} (Fig. S16†). Printed parts were washed with acetone to remove polymer not part of the cross-linked structure (see Fig. S17†) and dried under reduced pressure at ambient temperature.

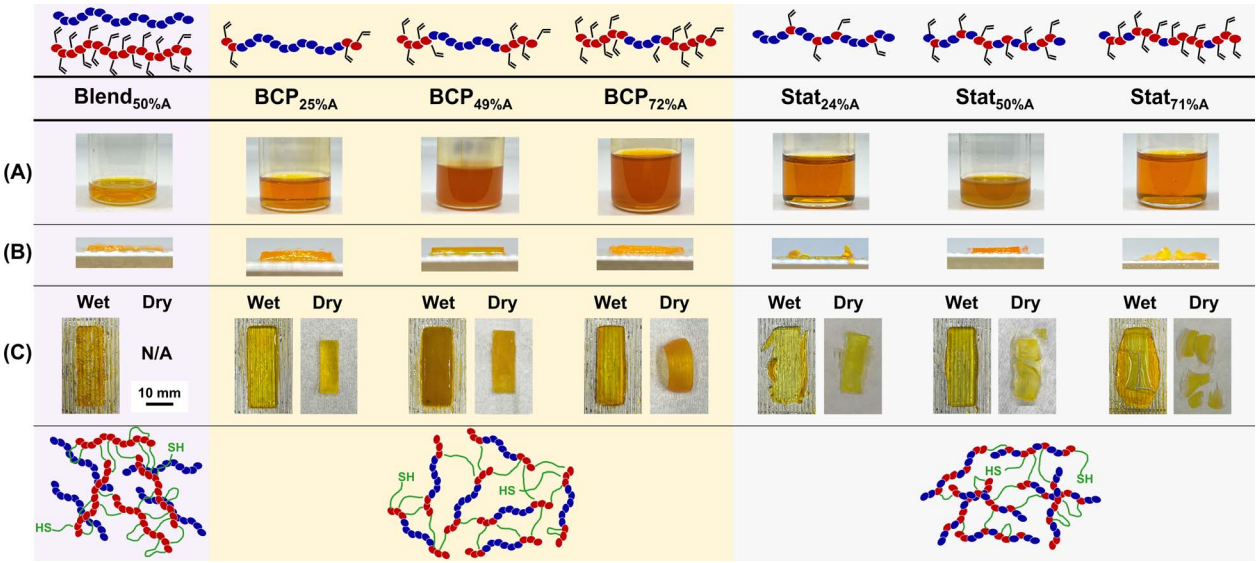

Fig. 3 Printing of resins composed of aPCs, photoinitiator, inhibitor, dye, and crosslinker by DLP. Images of (A) resin (vials are 27 mm), (B) wet print profile, (C) wet (left) and dry (right) prints for each resin. Wet prints are 10 mm × 30 mm. Dry print for X-Blend$_{50\%A}$ fragmented upon drying. Scale bar for (C) only.

Printed objects exhibited 20–38% shrinkage after drying due to the removal of solvent, as seen visibly in Fig. 3C. Shrinkage decreased with increasing mol% PVCHC (Fig. S18†), which is expected as the number of cross-linkable sites increased concurrently with mol% PVCHC, thereby increasing the crosslinking density. This was also supported by the swelling test in ethyl acetate which revealed that swelling ratio decreased with increasing mol% PVCHC (Table S5†).

The fidelity of the printed parts was characterized by optical (Fig. 3C) and SEM images (Fig. 4 and S19–S23†). All X-BCPs demonstrated good print integrity, X-Stats exhibited poor resolution and weak layer adhesion, and X-Blend$_{50\%A}$ was not printable (*e.g.*, only islands of solid and regions of liquid resin were present after drying). SEM images of the solid pieces for X-Blend$_{50\%A}$ revealed what appear to be aggregated polymer spheres on a bulk crosslinked network (Fig. 4A), which may occur because P$_{0\%A}$ is expelled upon formation of a crosslinked network given that P$_{0\%A}$ and P$_{100\%A}$ are not chemically attached to each other. In contrast, the excellent fidelity of all X-BCPs is evident from the optical images (Fig. 3B and C), with X-BCP$_{25\%A}$ reaching the resolution limit of the DLP (Fig. S24†). As shown in the SEM images of Fig. 4B–D, structural differences of print cross-section are evident based on BCP composition: X-BCP$_{25\%A}$ and X-BCP$_{72\%A}$ were smooth and had no obvious defects, whereas X-BCP$_{49\%A}$ showed inhomogeneities, both globular outlines on the surface and stratifications in the cross-sectional image, consistent with its more pronounced microphase separation.

Unlike BCPs, the statistical copolymers exhibited poor resolution during printing and severe delamination after drying. As seen in optical "wet" images in Fig. 3C, both X-Stat$_{24\%A}$ and X-Stat$_{71\%A}$ had poor print fidelity with X-Stat$_{71\%A}$ experiencing overcuring on the edges of the print; in contrast, X-Stat$_{50\%A}$ had decent resolution during printing. However, after washing and drying, X-Stat$_{24\%A}$ and X-Stat$_{50\%A}$ both exhibited large-scale delamination and X-Stat$_{71\%A}$ was brittle and fragmented. We posit that the statistical distribution of vinyl groups leads to the formation of a homogeneous network of crosslinks, in contrast to the BCPs which crosslinked in isolated areas due to phase separation. Consequently, if the statistical copolymer resins cure too quickly in a given layer, it cannot form crosslinks to the following layer, ultimately resulting in large-scale delamination and overcuring. Due to the poor fidelity of these prints, only X-Stat$_{50\%A}$ was imaged by SEM (Fig. 4E), revealing no apparent defects other than delamination. We note that print parameters may be optimized for the resins prepared with statistical copolymer, but it is noteworthy that all BCPs have good print fidelity under the same printing conditions, as desirable for rapid material evaluation. Thus, at the molecular level, polymer architecture greatly impacts the printability, while monomer ratio has negligible effect.

Thermal properties of printed objects

Crosslinking, as occurs during DLP, was expected to improve the thermal stability of the polymers, essentially turning a thermoplastic into a thermoset. To probe this, the printed samples were characterized by TGA. Fig. S25† and Table 2 show that all printed copolymers displayed a gradual mass loss of about 5–15 weight% in the range of 100–270 °C that we attribute to dangling bonds (*e.g.*, unreacted thiol groups). For all samples, T_d's increased by ~20–60 °C as expected for crosslinked networks (see Table S6† for a direct comparison of thermal properties of pristine and printed polymers). Notably, the thermal degradation profiles of X-Blend$_{50\%A}$ and X-P$_{100\%A}$ are very similar, indicating that P$_{100\%A}$ dominated the crosslinked network of the blend and that a majority of P$_{0\%A}$ was likely removed during printing and subsequent washing. For all

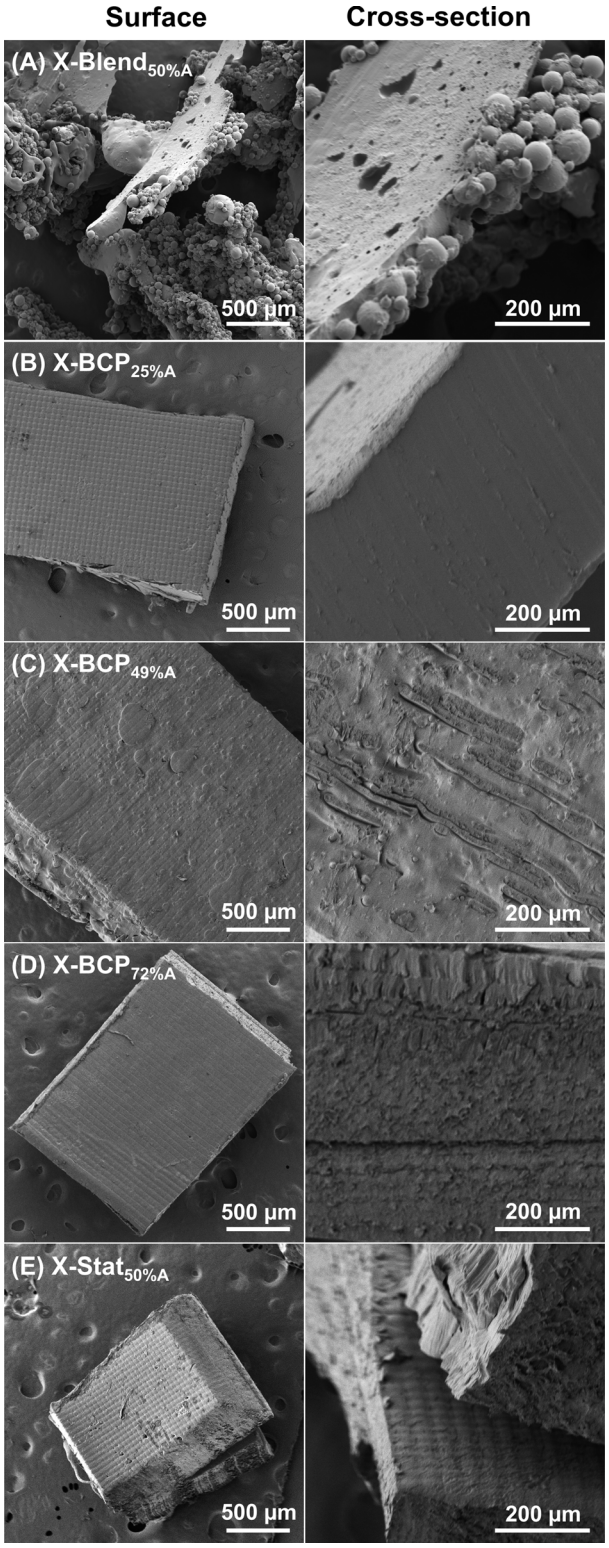

Fig. 4 SEM of surface (left) and cross-section (right) of each printed object after drying: (A) X-Blend$_{50\%A}$, (B) X-BCP$_{25\%A}$, (C) X-BCP$_{49\%A}$, (D) X-BCP$_{72\%A}$, and (E) X-Stat$_{50\%A}$.

polymers, mass loss at around ~315 °C is attributed to the degradation of the uncrosslinked and uncrosslinkable polymer (*i.e.*, unreacted PVCHC and PPC segments). The relative mass loss in this step is consistent with swelling ratio across polymers, with both values decreasing with increasing mol% PVCHC (Table S5†). The new weight loss step, occurring ~50 °C higher than the first, is attributed to degradation of the crosslinked network. As with the pristine polymers, both T_d's increased linearly with mol% PVCHC for X-BCPs and X-Stats, demonstrating that the monomer ratio dictates the trend in T_d for polymers of comparable M_n even after crosslinking. Regardless of polymer composition or architecture, all prints charred at ~450 °C, which is ~100 °C higher than the pristine polymers. Interestingly, the T_d's for X-Stats were all higher than the corresponding X-BCPs, consistent with swelling ratios, which were lower for X-Stats than for X-BCPs. These data support a slightly higher crosslink density for X-Stats, potentially due to the more homogeneous distribution of the VCHC in the polymer (and thus a more uniform distribution of crosslinks throughout the structure), reducing the size of swellable segments. Taken together, TGA data support that crosslinking improves the thermal stability of the aPCs, and both monomer ratio and polymer architecture affect printed object properties.

The thermal transitions of the printed objects were also analyzed by MDSC, with data shown in Fig. S26† and Table 2. For all printed parts, a T_g attributed to the PVCHC block was no longer observed, which is expected since these hard blocks are crosslinked and can no longer undergo long-range segmental motion. The T_g of the PPC block was observed for all prints with low to moderate mol% PVCHC, whereas X-BCP$_{72\%A}$, X-Stat$_{71\%A}$, and X-P$_{100\%A}$ did not have detectable T_g's. For all printed copolymers, the T_g of the PPC block decreased by 40–50 °C. This is likely due to the plasticizing effect of singly reacted thiol crosslinkers, whose presence is clearly seen in the TGA profiles (*vide supra*). In MDSC, the non-reversing heat flow identifies kinetic events such as enthalpic relaxation (endothermic peak) and curing reactions (exothermic peak).[54] Enthalpic relaxation measures the molecular relaxations within a polymer, typically occurring around the T_g of the polymer and reported as enthalpy recovery. All pristine polymers except BCP$_{72\%A}$ exhibited enthalpic relaxation, and their associated prints had comparable enthalpy recovery values (Fig. S26 and Table S6†); the exception to this is X-Blend$_{50\%A}$, which had an ~80% decrease in enthalpy recovery, indicating that much of P$_{0\%A}$ was removed, as supported by SEM images and TGA data. All polymers containing PVCHC had an exothermic peak at ~120–150 °C, demonstrating self-curing reactions at elevated temperatures likely due to vinyl–vinyl reactions.

Mechanical properties of printed objects

To demonstrate the effect of polymer composition and architecture on the mechanical properties of the printed objects, 10 × 30 × 1 mm^3 bars were printed and subjected to tensile and indentation measurements. The stress–strain profiles from DMA uniaxial tension tests are shown in Fig. 5A, with full-scale plots available in Fig. S27.† No data were collected for X-Blend$_{50\%A}$, X-Stat$_{24\%A}$, and X-Stat$_{71\%A}$ due to their poor bulk integrity, which caused the prints to crumble or fracture before analysis. For the X-BCPs, both tensile strength and Young's

Table 2 Thermal and mechanical properties of the printed structures

			DMA tensile test			Nanoindentation	
Polymer	T_g (°C)	T_d (°C)	Young's modulus (MPa)	ε_{break} (%)	σ_{max} (MPa)	Hardness (GPa)	Young's modulus (MPa)
X-$P_{100\%A}$	—	332, 369	N/A	N/A	N/A	>3.6	>58
X-$Blend_{50\%A}$	28	336, 364	N/A	N/A	N/A	N/A	N/A
X-$BCP_{25\%A}$	−7.9	301, 360[a]	16.2 ± 0.8	185 ± 14	0.79 ± 0.07	0.117 ± 0.004	6.6 ± 0.4
X-$BCP_{49\%A}$	2.5	310, 365	142 ± 2	86 ± 37	2.95 ± 0.22	1.0 ± 0.3	31 ± 2
X-$BCP_{72\%A}$	—	323, 369	349 ± 9	5 ± 2	6.77 ± 0.65	2.5 ± 0.3	51 ± 3
X-$Stat_{24\%A}$	5.0	313, 365[a]	N/A	N/A	N/A	0.018 ± 0.003	1.7 ± 0.2
X-$Stat_{50\%A}$	9.0	324, 384	2.93 ± 0.03	36 ± 10	0.58 ± 0.03	0.015 ± 0.001	0.58 ± 0.04
X-$Stat_{71\%A}$	—	334, 384	N/A	N/A	N/A	N/A	N/A

[a] Shoulder peak.

modulus increased linearly with increased mol% PVCHC, ranging from 0.80 to 6.80 MPa and 16 to 350 MPa, respectively (Table 2). Conversely, elongation at break decreased linearly from 185% to 5% (Fig. 5C and S28†). Only X-$Stat_{50\%A}$ demonstrated fully elastic behavior. The X-BCPs exhibited yield points at approximately 20%, 5%, and 3% strain with increasing mol% PVCHC, with X-$BCP_{72\%A}$ showing a slight necking behavior. This result contrasts with other reports of vat photopolymerization of aPCs, which typically report elastic deformation until break, likely due to the use of oligomeric aPCs (M = ~5 kDa or lower) and softer polymers (T_g < 40 °C).[33,35] These data illustrate that DLP of BCPs (M_n > 20 kDa) containing hard blocks provides access to tougher materials with plastic deformation dependent on monomer ratio.

Nanoindentation was also used to evaluate the performance of the prints under compressive force. In a typical experiment, a spherical tip with a radius of ~200 μm approached and pressed into the surface at a rate of 0.25 μm s^{-1}, held at a constant depth for 30 seconds, then unloaded and retracted from the surface. The applied load *versus* displacement plots for the X-BCPs, X-$Stat_{24\%A}$, and X-$Stat_{50\%A}$ are shown in Fig. 5B. Similar to the tensile test results, the compression strength of the X-BCPs increased linearly with increasing mol% PVCHC, with hardness values rising from 0.117 to 2.5 GPa and Young's modulus increasing from 6.6 to 51 MPa (Table 2). Although the Young's modulus from nanoindentation was significantly smaller than that measured under tension using DMA, both techniques showed a positive correlation with mol% PVCHC.

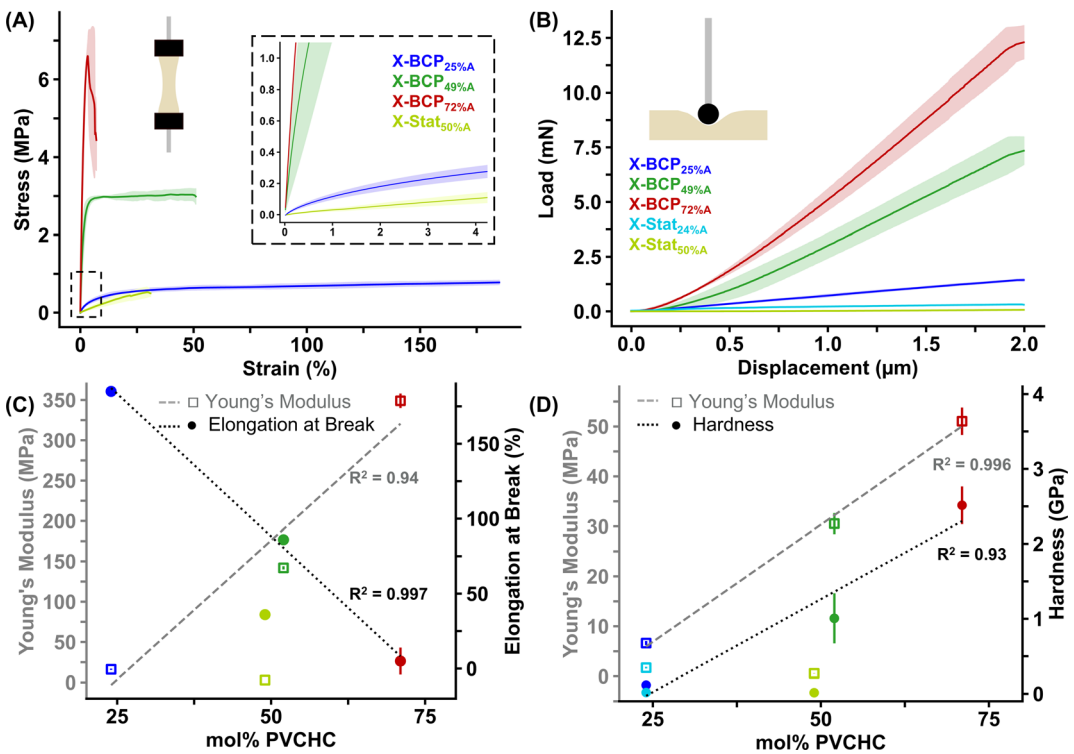

Fig. 5 Mechanical properties of each BCP and $Stat_{50\%A}$ printed objects. (A) Tensile stress/strain curve from DMA with a zoomed inset (n = 3); (B) nanoindentation plot of load *vs.* displacement (n = 3). (C) Tensile properties (Young's modulus and elongation at break) compared to mol% PVCHC. (D) Nanoindentation properties (Young's modulus and hardness) compared to mol% PVCHC.

Both X-Stat$_{24\%A}$ and X-Stat$_{50\%A}$ exhibited weaker mechanical properties than their X-BCP counterparts, with hardness values 1–2 orders of magnitude lower and significantly reduced Young's moduli (note: results may be skewed due to surface unevenness). Additionally, the relaxation behavior of the prints during the hold step was evaluated, shown by the load *versus* time plots in Fig. S29.† The X-BCPs exhibited decreasing percent relaxation with increasing mol% PVCHC, from 58% to 45% to 16% of the maximum load after a 30 seconds hold. X-Stat$_{24\%A}$ relaxed by 74%, and X-Stat$_{50\%A}$ by 42%, indicating again that relaxation is strongly correlated with mol% PVCHC. A summary of all mechanical properties is provided in Tables 2 and S7.†

BCPs generally have superior thermomechanical properties compared to their statistical copolymer analogues due to their better morphology control as demonstrated by Keeny and coworkers: the controlled architecture of BCPs allows for a more predictable and uniform morphology, in contrast to disordered structures of statistical copolymers which can also be unpredictable.[55] Our work supports this in the crosslinked networks. Although phase separation can also be realized in blends of homopolymers, this sample is not suitable for printing since the uncrosslinkable polymer (P$_{0\%A}$) is not integrated into the product. These findings demonstrate that bulk mechanical properties are intrinsically connected to microstructure which is dictated by polymer composition and architecture.

Hydrolysis study of the printed objects

A unique feature of aPCs is their ability to degrade into benign biocompatible byproducts and thus we evaluated the effect of polymer composition and architecture on degradation of printed structures. Initially, X-BCP$_{49\%A}$ was used as a representative sample and the hydrolytic degradation evaluated under various conditions, with results reported in Table S8 and Fig. S30.† In a pH 7.4 buffer at 37 °C, X-BCP$_{49\%A}$ showed only ~2% mass loss after two months, indicating good stability under physiological conditions. In contrast, under acidic conditions (0.5 N H_2SO_4 at 50 °C), X-BCP$_{49\%A}$ showed ~10% mass loss over 7 days, and under basic conditions (0.5 N NaOH at 50 °C) ~80% mass loss was observed in 7 days. This suggests that the degradation mechanism is base-catalyzed, consistent with previously reported polycarbonates.[56] The use of a swelling agent (THF) accelerated base hydrolysis,[57] allowing for complete degradation within 7 days, indicating that bulk hydrolysis facilitated by the swelling agent proceeds faster than surface erosion. The DLP prints thus had a much slower hydrolysis rate compared to the porous crosslinked aPC printed *via* DIW technique (complete hydrolysis in <1 day in basic media).[31] These differences highlight the complementarity of different AM techniques in controlling surface area and degradation profiles.

The effect of polymer composition on degradation rate was determined by subjecting different prints to the same hydrolysis conditions (0.5 N NaOH + THF at 50 °C). From the optical images, X-BCPs with higher mol% PVCHC had slower hydrolysis, with no printed part identifiable after 1, 2, and 4 days for X-BCP$_{25\%A}$, X-BCP$_{49\%A}$, and X-BCP$_{72\%A}$, respectively (Fig. 6 and Table S9†). This is consistent with differences in crosslinking of the sample as demonstrated by swelling ratio (*vide supra*) and aligns with other hydrolysis studies of crosslinked polymer networks.[58] Under such conditions, aPCs hydrolyze into their constituent diols and CO_2 gas, in this case yielding 4-vinylcyclohexene-1,2-diol (VCHD) and 1,2-propanediol (PD).[59] As shown in the photographs in Fig. 6, an oil phase is evident atop the basic aqueous solution after complete hydrolysis (by day 5 in all cases; this can be attributed to VCHD which is not miscible with water and separates as an organic phase floating on the water whereas PD is water-miscible and resides in the aqueous phase. Notably, the light orange color of the organic layer is attributed to the organo-soluble dye. The polymer architecture was found to play an important role in hydrolysis: X-Stats hydrolyzed slower than their X-BCP analogues

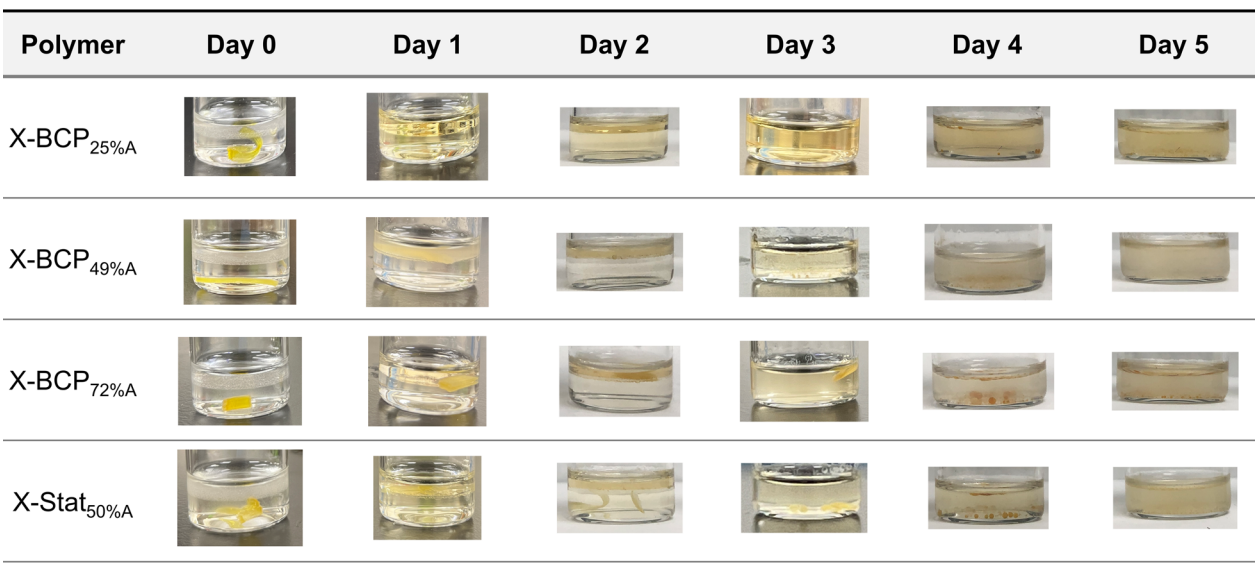

Fig. 6 Representative images of hydrolysis of each print over 5 days in 0.5 N NaOH with THF as a swelling agent. Each test was performed on three separate samples.

(Fig. S31†), illustrating that phase separation enabled by the BCP architecture may increase the rate of hydrolysis compared to the more homogenously distributed cross-links in the statistical copolymer. These results support that hydrolysis is governed by crosslinking density, with both monomer ratio and polymer architecture playing important roles.

^{1}H NMR spectroscopy was used to analyze the hydrolytic solutions of X-BCP$_{49\%A}$ and X-Stat$_{50\%A}$ over time. Both samples were submerged in 0.1 N NaOH and THF (1 : 1 v/v) at 50 °C with liquid components isolated at various time intervals, solvent removed, and solid redissolved in $CDCl_3$ and subjected to characterization by ^{1}H NMR. As shown in Fig. S32,† VCHD and PD were present in both samples, but with different evolution profiles. In X-Stat$_{50\%A}$, VCHD was detected after only one day, whereas in X-BCP$_{49\%A}$ it was only observed after 20 days; for both prints, PD was present at every time point. This suggests that in X-Stat$_{50\%A}$ the two types of repeat units hydrolyze at commensurate rates, since both linkages are evenly distributed throughout the polymer chains and are equally accessible. In contrast, the crosslinked domains in the X-BCPs are resistant to hydrolysis, leaving the non-crosslinked domains degrade first. Together with the finding that X-BCP$_{49\%A}$ hydrolyzed faster than X-Stat$_{50\%A}$, these results suggest that in the X-BCP network, uncrosslinkable PPC domains rapidly hydrolyze first, exposing a greater surface area for the bulk degradation of crosslinked PVCHC domains. This two-step process is faster than the surface erosion process of the uniform network composed of the statistical copolymer where all linkages are accessible. This understanding of the hydrolytic stability driven by polymer architecture and composition suggests the potential for fine-tuning degradation rates in tissue engineering applications.

Conclusion

In this study, we synthesized aPCs with varied compositions and architectures to explore the structure-processing-property relationships in the DLP process. SEM imaging and thermomechanical characterizations underscore the superiority of BCPs over both analogous statistical copolymers and homopolymer blends in both vat photopolymerization printability and property tunability. The BCPs were particularly notable for producing structurally robust printed objects with mechanical and thermal properties that could be adjusted by varying the monomer ratios. In contrast, the statistical copolymer samples exhibited delamination or fragmentation after printing and washing, and the homopolymer blend failed to yield an isolable structure. Furthermore, this study revealed that both the monomer ratio and sequence significantly influenced hydrolytic degradation rates of printed objects, with BCPs demonstrating a decelerated degradation as the percent PVCHC block increased, and the statical copolymers degrading more slowly than their corresponding BCPs. This research highlights the critical role of polymer composition and architecture in optimizing 3D printing processes and provides valuable insights for future work aiming to tailor polymer properties for specific applications. Ongoing and future studies will extend these findings to other polymer systems, offering a more comprehensive framework for designing advanced materials tailored for additive manufacturing.

Experimental section

Materials and instruments

All reactions were performed under an argon atmosphere using standard glovebox techniques. Glassware and stainless-steel reactors were dried at 150 °C for 24 h prior to use. Solvents were purchased from commercial sources and dried using the MBraun Manual Solvent purification system packed with Alcoa F200 activated alumina desiccant. (*R*,*R*)-(−)-*N*,*N*′-Bis(3,5-di-*tert*-butylsalicylidene)-1,2-cyclohexanediaminocobalt(II) (salenCo(II)) was purchased from Millipore-Sigma and oxidized to salenCo(III)TFA following a previously reported procedure.[60] Bis(triphenylphosphine)-iminiumtrifluoroacetate (PPNTFA) was purchased from Acros. Propylene oxide (99%, mix of isomers) and 4-vinyl cyclohexene oxide (98%, mix of isomers) were purchased from Alfa Aesar and dried over CaH_2 under reduced pressure prior to use. Propylene carbonate, ethyl acetate (>99.5%), phenylbis(2,4,6-trimethylbenzoyl)phosphine oxide (BAPO), and 2,2′-bipyridine-5,5′-dicarboxylic acid (bipy-DA) were purchased from Millipore-Sigma; 1,6-hexanedithiol (97%) was purchased from Alfa Aesar; 1,2,3-trihydroxybenzene was purchased from CHEM-IMPEX; and Sudan I was purchased from TCI Chemical, and all were used without further purification.

SEC was performed with a Tosoh HLC-8320 GPC using a refractive index (RI) detector and equipped with TSKgel Super HZ-M columns; THF was used as the mobile phase (50 °C, 0.1 mL min^{-1} flow rate, 2.0 mg mL^{-1} concentration). M_w and M_n were calculated using data from the RI detector calibrated against polystyrene standards. For FTIR spectroscopy, Jasco FT/IR-4600 with a diamond-coated ZnSe crystal was used in ATR mode. ^{1}H NMR spectra were recorded on a 400 MHz Bruker spectrometer at 25 °C operating at 399.66 MHz. Samples were prepared in $CDCl_3$ referenced against residual $CHCl_3$ at 7.26 ppm. Acquisition parameters were relaxation delays of 2 s with a 45° pulse. ^{1}H NMR DOSY spectra were recorded on a 500 MHz Varian spectrometer at 25 °C using the convection-corrected pulse sequence DBPPSTE_CC without spin. Samples were 3 mg mL^{-1} polymer in $CDCl_3$, dissolved overnight and added to oven-dried 5 mm NMR tubes. Spectra were collected in 15 increments for gradients from 71 to 1780, with diffusion gradient lengths of 3.6–4.4 ms and diffusion delays of 90–110 ms. Each FID had 16 scans, a 2 s relaxation delay, and a 90° pulse angle with 8 steady-state scans. M_w was calculated using calibration curve fit parameters $\nu = 0.46$ and $b' = -7.97$ m^2 s^{-1} as reported by Junkers and coworkers in eqn (1):[48]

$$\log(D) = b' - \nu \log(M_w) \quad (1)$$

Synthesis of polymers

Homopolymers: catalyst salenCo(III)TFA, cocatalyst PPNTFA, and epoxide monomer (PO or VCHO) were added to a stainless steel reactor in an argon glovebox, sealed, pressurized with 2 MPa dry

CO_2, and let stir 2 days at ambient temperature (PO) or 3 days at 45 °C (VCHO). BCPs: catalyst, cocatalyst, CTA bipy-DA, and PO monomer were added to a stainless steel reactor in an argon glovebox, sealed, pressurized with 2 MPa dry CO_2, and let stir two days at ambient temperature. VCHO was then added, the reactor was charged with CO_2, and let stir for 3 days at 45 °C. Statistical copolymers: catalyst, cocatalyst, PO, and VCHO were all added to a reactor, charged with 2 MPa dry CO_2, and let stir 2 days at ambient temperature. All polymers were purified by diluting with a minimal amount of dichloromethane and precipitating into acidic methanol (×3). Catalyst removal was verified by visual appearance (colorless when redissolved) and by ICP-MS of representative samples (<0.07 ppm cobalt in polymer sample).

Resin formulation

Polymers were dissolved in a binary solvent system comprising 3 : 1 v/v propylene carbonate and ethyl acetate at a polymer concentration of 450 mg mL^{-1}. Then, 1,6-hexanedithiol was incorporated in a stoichiometric ratio of 1 : 1 of thiol relative to the vinyl group, the latter estimated from the polymer M_n. Then, 0.5 wt% of the photoinitiator, phenylbis(2,4,6-trimethylbenzoyl) phosphine oxide (BAPO), 0.1 wt% of the radical inhibitor, 1,2,3-trihydroxybenzene, and 0.02 wt% of the dye, Sudan I, were introduced into the solution, all wt% relative to the total mass of the solvent, polymer, and thiol. To remove air bubbles, the resin was centrifuged at 2000 rpm for 5 minutes. Resins were prepared within 24 h of printing.

3D printing

All 3D printing was conducted using the commercial Flashforge Hunter DLP 3D printer, which employs a 405 nm projector. Structures were sliced in FlashDLPrint, the CAD software developed by Flashforge. 10 layers were printed for each object with a layer height of 100 μm for a total height of 1 mm. Using a 200% light intensity, the light exposure time was gradually reduced from 60 seconds to 55 seconds across 8 decremental time layers to control exposure. After printing, the scaffolds were removed from the build platform with a metal spatula and rinsed with acetone (×5) to eliminate uncured resin. All printed objects were directly dried under reduced pressure at room temperature for 24 h to remove any residual volatiles, without further post-curing process.

Characterizations

TGA analyses of the polymers were performed in a TA Instruments TGA 5500 under N_2 flow. 3–5 mg polymeric or 10–30 mg printed samples were heated on a platinum pan from room temperature to 100 °C at a rate of 20 °C min^{-1}, held isothermally for 10 min, then heated to 500 °C at a rate of 20 °C min^{-1}. MDSC was performed using a DSC 2500 (TA Instruments) in the modulated mode under a N_2 atmosphere. ∼5 mg of polymer sample was hermetically sealed in a pan and temperature was ramped from room temperature to 150 °C at 20 °C min^{-1} and held isothermally for 1 min to erase thermal history. Pans were then cooled to −60 °C at 20 °C min^{-1} and equilibrated for 10 min, then temperature was modulated at ±1.00 °C for 1 min prior to data collection at 2 °C min^{-1} from −60 °C to 150 °C. T_g was taken as the midpoint of the inflection tangent of the normalized reversing heat flow. Enthalpy recovery was defined as the integrated peak area from the normalized non-reversing heat flow. SEM images were taken with a TESCAN VEGA SEM with an accelerating voltage of 3–5 kV. Samples were attached to a conductive double-sided carbon tape and coated with 10 nm of gold prior to imaging. Optical images of the resins and printed objects were recorded using an iPhone X. Optical microscopy images were taken with AmScope M158C-2L-E1 with a 1.3 MP USB 2.0 camera at different magnifications.

DMA was carried out on a TA Instruments DMA 850 with a film clamp. The tensile tests were carried out at a speed of 3 mm min^{-1} under ambient conditions (22 ± 2 °C). Specimens for tensile testing were 10 × 30 × 1 mm^3 rectangles. All samples were evaluated in triplicate. Nanoindentation was carried out on a Bruker Hysitron Biosoft *in situ* Indenter with a 400 μm sapphire spherical tip under ambient conditions. A 3 × 3 × 1 mm^3 printed specimen was fixed to a glass slide for each experiment, and the tip was set to 2 μm from the surface. The tip approached the sample at 0.25 μm s^{-1} then loaded at 0.25 μm s^{-1} for 8 s until a total displacement of 2 μm, held for 30 s, and finally unloaded and retracted at 0.25 μm s^{-1}. Measurements for each material were collected in triplicate, sampling from different regions of the specimen. The elastic moduli were calculated based on the Herzian model using eqn (2), where δ is the total indentation depth, P is the applied load, E is the elastic modulus, and Poisson's ratio (0.4 for crosslinked polymers). Eqn (2) is fit by least squares to the loading data.

$$P = \frac{4E}{3(1-\nu^2)}\sqrt{R}\delta^{\frac{3}{2}} \quad (2)$$

The hardness was calculated on the unloading segment according to the Oliver & Pharr Method, using correction factors $\varepsilon = 0.75$ and $\beta = 1$ and the area function for a 200 μm radius conical probe using TriboQ Analytical App from Bruker.

Swelling experiments were carried out by adding ∼1 mL ethyl acetate to 2–10 mg samples of printed polymer for 24 h and comparing the initial dry mass (m_i) and swollen mass (m_s) after dabbing dry. Swelling ratio S was calculated according to the following equation:

$$S = \frac{m_s - m_i}{m_i} \times 100\% \quad (3)$$

Data availability

Data is available in the ESI.†

Author contributions

K. S. and C. H. contributed equally to this study; K. S., M. S., and N. A. synthesized polymers; K. S. characterized polymers; C. H. optimized and performed DLP 3D printing; M. K. and T. W. provided a vat for 3D printing; K. S., C. H., and P. W. characterized thermal and mechanical properties of prints; C. H. and P. W. conceptualized and performed hydrolysis studies; K. S. was primary writer of the manuscript; C. H., P. W., and E. P.

were primary editors of the manuscript; D. D., E. P., and P. W. conceived the idea. All authors discussed the results and provided feedback on the manuscript.

Conflicts of interest

The authors declare no conflict of interest.

Acknowledgements

We thank Ciera Cipriani and Yunchong Yang for their help with setting up the printing parameters. We thank Radhika Laxminarayana and Michael Fitzl from Bruker Nano Surfaces Division for their assistance in nanoindentation analysis. Use of the Texas A&M University Soft Matter Facility (RRID:SCR_022482) is acknowledged. The authors gratefully acknowledge the financial support of this work through research grants by the Welch Foundation (A-0923) to D. J. D. K. S. is supported by a NSF Graduate Research Fellowship Award #2139773.

References

1 J. Feng, R.-X. Zhuo and X.-Z. Zhang, *Prog. Polym. Sci.*, 2012, **37**, 211–236.
2 Y. Liu and X. Lu, *J. Polym. Sci.*, 2022, **60**, 3256–3268.
3 H. Cao and X. Wang, *SusMat*, 2021, **1**, 88–104.
4 P. Wei, G. A. Bhat and D. J. Darensbourg, *Angew. Chem., Int. Ed.*, 2023, **62**, e202307507.
5 W. Yu, E. Maynard, V. Chiaradia, M. C. Arno and A. P. Dove, *Chem. Rev.*, 2021, **121**, 10865–10907.
6 R. Poręba, M. Špírková, L. Brožová, N. Lazić, J. Pavličević and A. Strachota, *J. Appl. Polym. Sci.*, 2013, **127**, 329–341.
7 K. Dimitrov, D. Todorova, S. Nenkova and M. Herzog, *J. Chem. Technol. Metall.*, 2017, **52**(1), 28–40.
8 S. Matsumura, Y. Soeda and K. Toshima, *Appl. Microbiol. Biotechnol.*, 2006, **70**, 12–20.
9 S. Ye, S. Wang, L. Lin, M. Xiao and Y. Meng, *Adv. Ind. Eng. Polym. Res.*, 2019, **2**, 143–160.
10 Y. Wang, J. Fan and D. J. Darensbourg, *Angew. Chem., Int. Ed.*, 2015, **54**, 10206–10210.
11 J. Hilf, P. Schulze and H. Frey, *Macromol. Chem. Phys.*, 2013, **214**, 2848–2855.
12 S. Agarwal, M. Puchner, A. Greiner and J. H. Wendorff, *Polym. Int.*, 2005, **54**, 1422–1428.
13 J. Zhang, H. Qi, H. Wang, P. Hu, L. Ou, S. Guo, J. Li, Y. Che, Y. Yu and D. Kong, *Artif. Organs*, 2006, **30**, 898–905.
14 G.-W. Yang, Y.-Y. Zhang, Y. Wang, G.-P. Wu, Z.-K. Xu and D. J. Darensbourg, *Macromolecules*, 2018, **51**, 1308–1313.
15 K. C. Poon, M. Segal, A. J. Bahnick, Y. M. Chan, C. Gao, M. L. Becker and C. K. Williams, *Angew. Chem., Int. Ed.*, 2024, e202407794.
16 B. Grignard, S. Gennen, C. Jérôme, A. W. Kleij and C. Detrembleur, *Chem. Soc. Rev.*, 2019, **48**, 4466–4514.
17 G. A. Bhat and D. J. Darensbourg, *Green Chem.*, 2022, **24**, 5007–5034.
18 Y. Wang and D. J. Darensbourg, *Coord. Chem. Rev.*, 2018, **372**, 85–100.
19 G. L. Gregory, H. Gao, B. Liu, X. Gao, G. J. Rees, M. Pasta, P. G. Bruce and C. K. Williams, *J. Am. Chem. Soc.*, 2022, **144**, 17477–17486.
20 J. Liu, M. Jia, Y. Gnanou and X. Feng, *Macromolecules*, 2023, **56**, 1615–1624.
21 S. Ye, W. Wang, J. Liang, S. Wang, M. Xiao and Y. Meng, *ACS Sustain. Chem. Eng.*, 2020, **8**, 17860–17867.
22 S. C. Ligon, R. Liska, J. Stampfl, M. Gurr and R. Mülhaupt, *Chem. Rev.*, 2017, **117**, 10212–10290.
23 M. A. Geven, A. Lapomarda, O. Guillaume, C. M. Sprecher, D. Eglin, G. Vozzi and D. W. Grijpma, *Eur. Polym. J.*, 2021, **147**, 110335.
24 M. A. Geven, V. Varjas, L. Kamer, X. Wang, J. Peng, D. Eglin and D. W. Grijpma, *Polym. Adv. Technol.*, 2015, **26**, 1433–1438.
25 M. A. Geven, C. Sprecher, O. Guillaume, D. Eglin and D. W. Grijpma, *Polym. Adv. Technol.*, 2017, **28**, 1226–1232.
26 S. B. G. Blanquer, M. Werner, M. Hannula, S. Sharifi, G. P. R. Lajoinie, D. Eglin, J. Hyttinen, A. A. Poot and D. W. Grijpma, *Biofabrication*, 2017, **9**, 025001.
27 S. Schüller-Ravoo, E. Zant, J. Feijen and D. W. Grijpma, *Adv. Healthcare Mater.*, 2014, **3**, 2004–2011.
28 I. A. Barker, M. P. Ablett, H. T. J. Gilbert, S. J. Leigh, J. A. Covington, J. A. Hoyland, S. M. Richardson and A. P. Dove, *Biomater. Sci.*, 2014, **2**, 472–475.
29 S. Schüller-Ravoo, J. Feijen and D. W. Grijpma, *Macromol. Biosci.*, 2011, **11**, 1662–1671.
30 S. XiaoHui, L. Wei, S. PingHui, S. QingYong, W. QingSong, S. YuSheng, L. Kai and L. WenGuang, *Int. J. Adv. Manuf. Technol.*, 2015, **81**, 15–25.
31 P. Wei, G. A. Bhat, C. E. Cipriani, H. Mohammad, K. Schoonover, E. B. Pentzer and D. J. Darensbourg, *Angew. Chem., Int. Ed.*, 2022, **61**, e202208355.
32 A. Bagheri and J. Jin, *ACS Appl. Polym. Mater.*, 2019, **1**, 593–611.
33 T. Brossier, G. Volpi, J. Vasquez-Villegas, N. Petitjean, O. Guillaume, V. Lapinte and S. Blanquer, *Biomacromolecules*, 2021, **22**, 3873–3883.
34 Y.-Y. Zhang, G.-P. Wu and D. J. Darensbourg, *Trends Chem.*, 2020, **2**, 750–763.
35 A. C. Weems, M. C. Arno, W. Yu, R. T. R. Huckstepp and A. P. Dove, *Nat. Commun.*, 2021, **12**, 3771.
36 F. S. Bates, *Science*, 1991, **251**, 898–905.
37 F. S. Bates and G. H. Fredrickson, *Phys. Today*, 1999, **52**, 32–38.
38 B. Weidinger, G. Yang, N. Von Coelln, H. Nirschl, I. Wacker, P. Tegeder, R. R. Schröder and E. Blasco, *Adv. Sci.*, 2023, **10**, 2302756.
39 S. Goyal, A. Yesu and S. S. Banerjee, *Polym. Eng. Sci.*, 2023, **63**, 3708–3718.
40 N. Verma, P. Awasthi, P. M. Pandey and S. S. Banerjee, *J. Appl. Polym. Sci.*, 2022, **139**, e53039.
41 C. J. Pless, S. Nikzad, I. Papiano, S. Gnanadass, F. B. Kadumudi, A. Dolatshahi-Pirouz, C. E. Thomsen and J. U. Lind, *Adv. Electron. Mater.*, 2023, **9**, 2201173.
42 A. Malafronte, I. W. Hamley, D. Hermida-Merino, F. Auriemma and C. De Rosa, *Polymer*, 2021, **237**, 124360.

43 R. Chen, J. Cai, K. C. H. Chin, S. Wang, A. J. Boydston, R. Thevamaran and P. Gopalan, *Giant*, 2024, **17**, 100204.
44 H. M. Pan, J. Sarkar and A. Goto, *ACS Appl. Polym. Mater.*, 2022, **4**, 8676–8683.
45 S. O. Catt, M. Hackner, J. P. Spatz and E. Blasco, *Small*, 2023, **19**, 2300844.
46 D. J. Darensbourg and W.-C. Chung, *Polyhedron*, 2013, **58**, 139–143.
47 S. Viel, M. Mazarin, R. Giordanengo, T. N. T. Phan, L. Charles, S. Caldarelli and D. Bertin, *Anal. Chim. Acta*, 2009, **654**, 45–48.
48 P. Voorter, A. McKay, J. Dai, O. Paravagna, N. R. Cameron and T. Junkers, *Angew. Chem.*, 2022, **134**, e202114536.
49 W. Jakubowski, A. Juhari, A. Best, K. Koynov, T. Pakula and K. Matyjaszewski, *Polymer*, 2008, **49**, 1567–1578.
50 P. C. Hiemenz and T. Lodge, *Polymer chemistry*, CRC Press, Boca Raton, 2nd edn, 2007.
51 T. G. Fox, *Bull. Am. Phys. Soc.*, 1956, **1**, 123.
52 Research Triangle Institute and Science Applications International Corporation, *Environmental Profile for Propylene Carbonate*, U.S. Environmental Protection Agency, Washington, D.C., EPA/600/R-98/068, 1998.
53 U.S. EPA, *Provisional Peer-Reviewed Toxicity Values for Ethyl Acetate*, U.S. Environmental Protection Agency, Washington, DC, EPA/690/R-13/013F, 2013.
54 P. Gabbott, in *Principles and Applications of Thermal Analysis*, ed. P. Gabbott, Wiley, 1st edn, 2008, pp. 1–50.
55 J. F. Kenney, *Polym. Eng. Sci.*, 1968, **8**, 216–226.
56 J. H. Jung, M. Ree and H. Kim, *Catal. Today*, 2006, **115**, 283–287.
57 A. Oesterreicher, J. Wiener, M. Roth, A. Moser, R. Gmeiner, M. Edler, G. Pinter and T. Griesser, *Polym. Chem.*, 2016, **7**, 5169–5180.
58 T. R. Yeazel-Klein, A. G. Davis and M. L. Becker, *Adv. Mater. Technol.*, 2023, **8**, 2201904.
59 B. Amsden, *Macromol. Biosci.*, 2021, **21**, 2100085.
60 A. Berkessel and M. Brandenburg, *Org. Lett.*, 2006, **8**, 4401–4404.